Correlating the 3D morphology of polymer-based battery electrodes with effective transport properties

Benedikt Prifling[1,*], Lukas Fuchs[1,*], Aigerim Yessim[2], Markus Osenberg[3], Melanie Paulisch-Rinke[3], Philip Zimmer[4,5,6], Martin D. Hager[4,5,6], Ulrich S. Schubert[4,5,6], Ingo Manke[3,6], Thomas Carraro[2], Volker Schmidt[1]

May 3, 2024

Polymer-based batteries represent a promising candidate for next-generation batteries due to their high power densities, decent cyclability and environmentally friendly synthesis. However, their performance essentially depends on the complex multi-scale morphology of their electrodes, which can significantly affect the transport of ions and electrons within the electrode structure. In this paper, we present a comprehensive investigation of the complex relationship between the three-dimensional (3D) morphology of polymer-based battery electrodes and their effective transport properties. In particular, focused ion beam scanning electron microscopy (FIB-SEM) is used to characterize the 3D morphology of three polymer-based electrodes which differ in material composition. The subsequent segmentation of FIB-SEM image data into active material, carbon-binder domain and pore space enables a comprehensive statistical analysis of the electrode structure and a quantitative morphological comparison of the electrode samples. Moreover, spatially resolved numerical simulations allow for computing effective properties of ionic and electronic transport. The obtained results are used for establishing analytical regression formulas which describe quantitative relationships between the 3D morphology of the electrodes and their effective transport properties. To the best of our knowledge, this is the first time that the 3D structure of polymer-based battery electrodes is quantitatively investigated at the nanometer scale.

Keywords: Polymer-based battery; Electrode; FIB-SEM tomography; Nanostructure; Statistical image analysis, Effective charge transport; Structure-property relationship

[1]Institute of Stochastics, Ulm University, 89069 Ulm, Germany
[2]Institute of Modelling and Computational Science, Applied Mathematics, Helmut-Schmidt-Universität/Universität der Bundeswehr Hamburg, 22043 Hamburg, Germany
[3]Institute of Applied Materials, Helmholtz-Zentrum Berlin für Materialien und Energie, 14109 Berlin, Germany
[4]Laboratory of Organic and Macromolecular Chemistry (IOMC), Friedrich Schiller University Jena, 07743 Jena, Germany
[5]Center for Energy and Environmental Chemistry (CEEC), Friedrich Schiller University Jena, 07743 Jena, Germany
[6]Helmholtz Institute for Polymers in Energy Applications Jena (HIPOLE), 07743 Jena, Germany
[*]Both authors contributed equally.

1 Introduction

The recent technological progress regarding electric vehicles, portable devices and consumer electronics leads to increasingly demanding requirements for state-of-the-art batteries. Nowadays, the most commonly used type of batteries are lithium-ion batteries due to their low self-discharge rate, high power density and decent energy density [1, 2]. However, ecological and environmental aspects are of major importance with regard to next-generation battery technologies. In particular, organic active materials have the potential to overcome the disadvantages of classical lithium-ion batteries, namely a limited availability of the raw materials, a high toxicity and detrimental effects on the environment [3–5]. Moreover, polymer-based batteries with organic active materials exhibit high-rate capabilities [6] and can be realized in a flexible design [7], which enables the usage of polymer-based battery electrodes for small portable devices with a low energy consumption. In particular, a Ragone plot can be used to set the polymer-based thin film technology into context with other energy storage systems such as the dominating lithium ion technology and supercapacitors [8, 9]. Comparing polymer-based batteries, supercapacitors and the classical lithium-ion technology, the latter offers the highest energy density, whereas supercapacitors enable the highest power density. In view of the Ragone plot, polymer-based batteries are situated in between those two technologies, which makes them - among others - favorable for acting as dampening element in hybrid storage systems extenuating high charging rates with a reasonable energy density.

In particular, poly(2,2,6,6-tetramethyl-4-piperinidyl-*N*-oxylmethacrylate) (PTMA) is one of the most investigated redox-active polymer since the early work at the beginning of the 2000s [10, 11]. This pioneering work set the basis for research into organic materials for energy storage solutions. The specific properties of PTMA, such as its high redox activity and stability, attracted the attention of researchers and industry to this technology and led to a growing interest in its commercial applications. In 2012 NEC tried to commercialize the first organic radical battery to power computers in case of power failure to prevent data loss [12]. Recently, Evonik sold their material technology TAeTTOOz® to InnovationLab [13]. In general, the aim of these technologies is the development of a printable flexible polymer battery. For this purpose, quantifying relationships between the morphology of polymer-based battery electrodes and the resulting electrochemical performance is crucial. More precisely, a quantitative analysis of ionic and electronic transport processes in battery electrodes based on organic materials is critical since these are likely to be a limiting factor for the cell performance as in the case of classical lithium-ion batteries [14–21].

A first quantitative investigation of the 3D structure of polymer-based electrodes via synchrotron tomography has shown a significant influence of the manufacturing processes on the resulting electrode microstructure [22]. The present paper realizes a further step towards a systematic analysis of the 3D morphology of polymer-based electrodes, using focused ion beam scanning electron microscopy (FIB-SEM). To the best of our knowledge, this is the first time that the three-dimensional structure of this kind of battery electrodes is quantitatively investigated with such a high resolution. In particular, this goes far beyond the use of conventional 2D SEM as described in [23], since imaging via 2D SEM only allows a qualitative morphological analysis, whereas the 3D FIB-SEM tomography as applied in the present study enables a detailed analysis of the three-dimensional electrode structure including a precise depiction of the electronic transport network on the nanoscale as well as the paths within the nanoporous network, which significantly influence ionic transport.

Note that the electrolyte in the porous electrodes serves as a reservoir for the ions required for the redox-reaction that ensures charge neutrality. As far as electronic transport is concerned, a minimum amount of electronically conductive additives must be ensured to provide complete percolation through the entire electrode thickness to guarantee the activation of all active material particles. Once this amount is reached, no further conductive additives should be added to achieve an optimum specific

capacity. More precisely, the percolation threshold is at 8 wt.-% SuperP according to [23], where polymer-based electrodes with varying fractions of SuperP are investigated via conductivity impedance measurements. In particular, it has been shown that there is no electrochemical activity below this percolation threshold, while a range of capacity utilization values can be achieved above the percolation threshold. This can be interpreted as follows: A minimum percolation path is required to ensure proper contact within the electronic transport network and to trigger electrochemical activities, but the amount of SuperP is not sufficient to activate all PTMA particles. By increasing the amount of SuperP, the maximum achievable absolute capacity is increased until a saturation value is reached, which is equals the amount of PTMA. For the purpose of investigating quantitative structure-property relationships, three different electrode compositions with a content between 30 and 60 wt.-% of SuperP have been chosen to ensure a well-percolated electrode that also exhibits a high capacity utilization as shown in [23].

In the present paper, the investigation of the electrodes considered in [23] is extended to charge transport processes, which are typically characterized by so-called effective transport coefficients [24]. In the context of porous electrodes, these characteristics are used to quantitatively describe the transport of ions or electrons in the porous medium whose morphology varies at the microscopic level. In particular, they represent the average/macroscopic behavior of transport phenomena and are essential for understanding and predicting the electrochemical performance of the electrodes. A key quantity often exploited to determine effective transport coefficients is effective tortuosity [22, 25–27], which is used as scaling factor for the ionic diffusion and electronic conductivity coefficients to obtain an effective coefficient that can be applied in mesoscopic and macroscopic models. Note that effective tortuosity is used in a similar way to scale both Fick's diffusion processes and the electronic transport of charged particles. In addition, effective transport coefficients can be applied in homogenized, physics-based electrochemical models like the pseudo two-dimensional (P2D) electrochemical model used in the context of conventional lithium-ion batteries, which is based on the pioneering work of Doyle, Fuller and Newman [28–32]. Recently, a modified Doyle-Fuller-Newman model has been derived for PTMA-based battery electrodes to describe charge transport processes in a dual-ion battery [33, 34]. Furthermore, cell design for such polymer-based batteries has been experimentally studied and supported by mathematical modeling [33, 34]. The present paper aims to provide a quantitative understanding of effective transport properties and their dependence on the 3D morphology of the electrode on the nano-scale. It will serve as basis for future research activities which make use of mathematical modeling and simulations, supporting the design of polymer-based battery electrodes with improved electrochemical properties.

The rest of this paper is organized as follows. Section 2 explains materials and methods considered in this paper, including a description of the manufacturing procedure of the three polymer-based electrodes with PTMA as active material (Section 2.1), and the subsequent imaging via 3D FIB-SEM tomography (Section 2.2). Then, in Section 2.3, the segmentation of the 3D image data into active material, carbon-binder domain (consisting of the conductive additive SuperP and the binder CMC, also referred to as SuperP phase in the following) and pore space is described. Afterwards, in Section 2.4, various geometrical descriptors are explained which are used to characterize the 3D morphology of the electrodes, whereas Section 2.5 contains a description of spatially-resolved numerical simulations of effective transport properties that are closely related to the electrochemical performance of the electrodes. Section 3 contains the results which have been obtained in the present paper. In particular, in Section 3.1, the differences between the nanostructures of the three electrode samples are statistically analyzed. Next, in Section 3.3, relationships between the 3D nanostructure of the polymer-based battery electrodes and effective transport properties are investigated by means of analytical regression formulas. Finally, Section 4 concludes and provides an outlook on possible future research.

2 Materials and methods

To begin with, we explain materials and methods considered in this paper. In particular, Section 2.1 describes the procedure which has been used for the manufacturing of three different polymer-based battery electrodes. Next, Section 2.2 explains how these samples are imaged by means of 3D FIB-SEM tomography. The segmentation of the resulting 3D image data into active material, carbon-binder domain and pore space is described in Section 2.3, whereas in Section 2.4, various geometrical descriptors are presented which are used to characterize the 3D morphology of the electrodes. Finally, Section 2.5 contains a description of numerical methods for computing effective charge transport properties.

2.1 Material synthesis and electrode manufacturing

Carbon black, Super P® Conductive, 99+% (metals basis) (Alfa Aesar, USA) and carboxymethyl cellulose (CMC) (Sigma Aldrich, USA) were purchased and used without further purification. PTMA was prepared via emulsion polymerization according to the synthesis procedure described in [35], where in the present study the particle type P2 from [35] is considered, consisting of nanoparticles with a mean particle size of 73 nm.

Furthermore, the manufacturing process of the polymer-based electrodes considered in the present paper is described in detail in [35]. A short summary of the main processing steps is provided here for convenience. In particular, we consider three electrodes that differ with regard to their material composition. The different ratios of PTMA, SuperP and CMC are listed in Table 1, where the sample name corresponds to the weight percentage of SuperP. The materials with a total weight of 500 mg for each fraction were dispersed in 5 mL water at 1,500 revolutions per minute for one hour with a disperser, Zentrimix 380 R (Andreas Hettich GmbH & Co, Germany). A doctor-blading setup of BYK, byko-drive XL, was used for film manufacturing. For this purpose, the slurry was doctor-bladed on aqueous KOH etched aluminum foil with a blade gap adjusted to 200 µm height at a casting speed of 250 mm s^{-1}. Coated films were annealed for 18 h at 80 °C under ambient atmosphere. The annealed electrodes exhibit thicknesses ranging from 70 µm to 150 µm, in consequence of the different slurry viscosity values for the electrodes hereafter referred to as SP30, SP45 and SP60. Electrodes of 15 mm diameter were punched with an MTI Corporation crimper (electrode area: 1.76 cm^2). Electrodes exhibit a loading of 1 to 3 mg after drying.

Material Sample	SP30	SP45	SP60
PTMA / $wt.-\%$	65	50	35
SuperP / $wt.-\%$	30	45	60
CMC / $wt.-\%$	5	5	5

Table 1: Material composition of three organic radical battery electrodes with different amounts of active material PTMA and conductive additive SuperP.

2.2 Tomographic imaging

In this section, we describe the sample preparation and imaging of the samples via 3D FIB-SEM tomography [36, 37]. Each of the three polymer electrodes was first cut into 1×3 mm sections with a scalpel and fixed to a standard aluminum SEM holder using a carbon adhesive pad. They were then

sputtered with a layer of gold approximately 10 nm thick to further improve the electronic conductivity at the sample surface. Infiltration with fillers such as resins or silicone was avoided. On the one hand, this was due to the concern that infiltration would significantly alter the structures to be measured. On the other hand, the infiltration of polymers creates a contrast problem, which in turn makes it difficult to distinguish between the sample and the infiltration material. Finally, without infiltration it is possible to increase the speed of cutting the sample with the focus ion beam, which results in a shorter measurement time. The samples were then transferred to the FIB-SEM, a ZEISS Crossbeam 340 at the Centre for Correlative Microscopy and Spectroscopy (CCMS). The crossbeam has a Gemini I electron column that was operated at a low voltage of 1 keV for the tomography imaging measurements. The low voltage was chosen to minimize the penetration depth of the primary electrons, which avoids the occurrence of artifacts. Moreover, the low voltage simplifies the segmentation of the resulting image data since the shallow depth of field means that areas that are not in the slice plane quickly become blurred. The gallium ion gun of the crossbeam, mounted at an angle of 54° to the electron column, was operated at an acceleration voltage of 30 keV. To obtain a good view of the area of the sample that is to be imaged, an area of approximately 40 µm × 40 µm was first removed from the sample using a gallium current of 30 nA. For sequential image acquisition, both the secondary electron in-lens detector integrated in the electron column and the detector built into the side of the microscope chamber, which also detects secondary electrons, were used. After polishing the side of the previously exposed area intended for tomography with a gallium current of 700 pA and setting the tilt compensation and dynamic focus, the serial sectioning process of the tomography was started. The cutting depth and pixel size were always chosen to be the same. More precisely, a pixel size of 15 nm is used in case of the samples SP30 and SP45. Due to a new gallium source, allowing for a longer measurement, a pixel size of 10 nm was used for the sample SP60. The sizes in numbers of voxels in each spatial direction of the three reconstructed samples are reported in Table 2.

Sample	x [num. voxels]	y [num. voxels]	z [num. voxels]
SP30	1237	700	1891
SP45	1796	700	880
SP60	2924	2122	1397

Table 2: Sample size in $x-$, $y-$ and z-direction, respectively. Note that the y-direction corresponds to the direction from the current collector to the separator, which is the main direction of ionic and electronic transport.

2.3 Image processing

In the following, we explain how the raw FIB-SEM image data is segmented into active material (PTMA), the carbon-binder domain (consisting of SuperP and CMC, called SuperP phase) and pore space. After completing tomographic imaging described in Section 2.2, the raw data was prepared for classification using the software Fiji [38]. First, the SIFT-based image drift correction was applied [39]. The data was then denoised by applying a 2D non-local means filter [40]. Due to the non-infiltrated nature of the measurement, the shine through artifacts, which represent the background of the sample in areas with no material in the cutting plane, had to be detected and removed. A U-net based 3D neural network was used for this challenging post-processing step [41]. The network was trained on many similar previous measurements not directly related to the present paper, which were classified using a random forest approach [42]. The removal of shine through artifacts using neural networks worked well for the samples SP45 and SP60. However, the sample SP30 showed many charging artifacts that the network had not been previously trained on, causing the network to fail.

Therefore, the previously mentioned random forest approach was used. Here, both input channels, the InLens detector signal and the angled chamber detector signal, were used to manually train a new random forest classifier using the ilastik software package [43]. Although much slower than the neural network approach, this ultimately resulted in a satisfactory removal of the shine through artifacts.

The resulting binary spatial information then had to be further classified into the active PTMA phase and the SuperP phase. For this purpose, a morphological approach was chosen, where we used the fact that the SuperP phase consists of very small clustered particles, compared to the PTMA phase. Based on this knowledge, a local thickness filter that is included in the Fiji software package was applied [38]. The result was then thresholded into the two remaining phases [44]. The segmentation procedure and the resulting segmented 3D images are visualized in Figures 1 and 2, respectively.

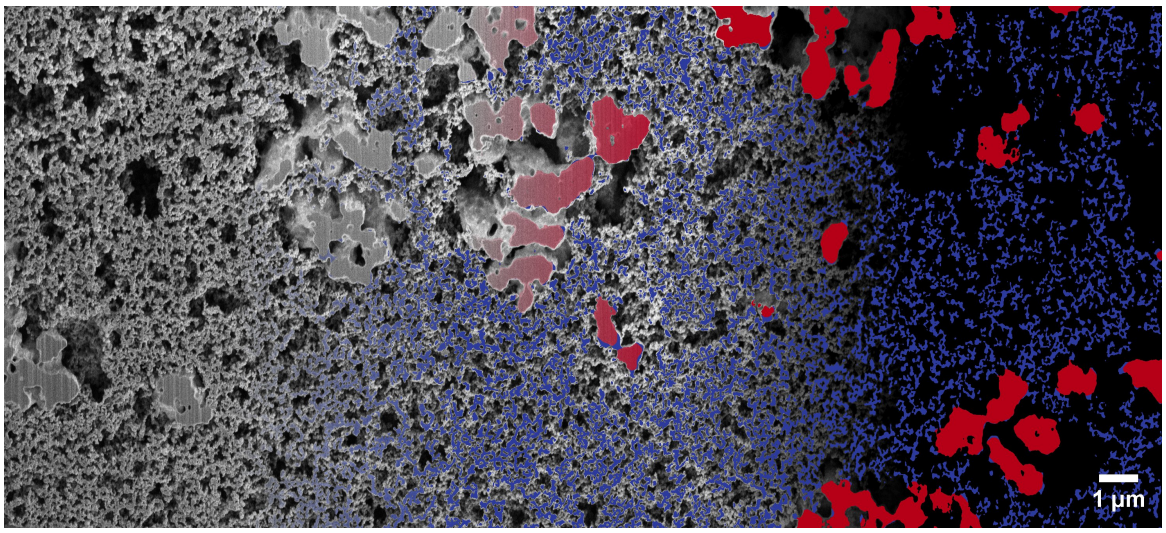

Figure 1: Exemplary selected 2D slice of sample SP60. From left to right, a continuous transition is shown from the grayscale SEM image to the segmentation into active material (red), SuperP phase (blue) blue and pore space (black).

.

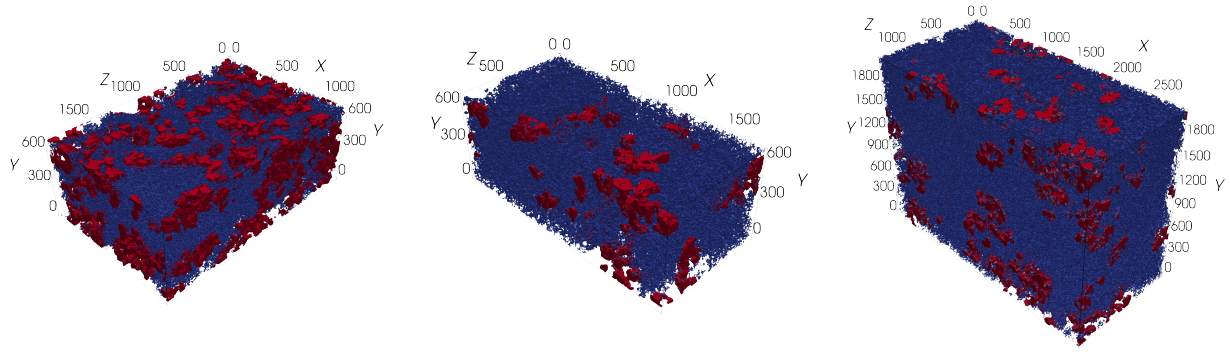

Figure 2: Visualization of the segmented 3D images. The PTMA phase is shown in red, the union of SuperP and CMC phase is shown in blue, and the pore space is kept transparent. The axis scale is in voxel, where the samples on the left (SP30) and in the middle (SP45) have a voxel size of 15 nm. The sample displayed on the right (SP60) has a voxel size of 10 nm.

2.4 Geometrical descriptors

In the following, several geometrical descriptors are briefly explained, which are used to characterize the 3D morphology of the polymer-based battery electrodes. Note that a superscript is used to refer to the phase for which the geometrical descriptor is computed. In particular, the superscripts AM (short for active material), SP (short for SuperP) and P (short for pore space) are used to refer to the PTMA phase, the carbon-binder domain (i. e. the union of SuperP and CMC) and the pore space, respectively. Furthermore, the superscript is omitted in case when the underlying phase is clear from the context.

Volume fraction. One of the most fundamental geometrical descriptors is the volume fraction $\varepsilon \in [0,1]$ of the phase under consideration. This quantity is estimated from 3D image data by the well-known point-count method [45]. Besides the globally computed volume fraction ε, the heterogeneity of the electrode nanostructures will be quantified by computing the volume fraction for non-overlapping cutouts of size $100\,\mu\text{m} \times 100\,\mu\text{m} \times 100\,\mu\text{m}$.

Specific surface area. In addition to porosity, we consider the specific surface area, which will be denoted by S. It is defined as the surface area between the considered phase and its complement divided by the volume of the sampling window. This quantity is estimated from voxelized 3D image data using an approach presented in [46], which is based on a convolution of the image with a $2 \times 2 \times 2$ kernel. Moreover, the specific surface areas of the different phases will be used to define more sophisticated geometrical descriptors as described in the next paragraph.

Interfaces. Besides the specific surface areas of the three phases, we consider the specific area of the interface between active material and the carbon-binder domain, denoted by $S^{\mathsf{AM}\cap\mathsf{SP}}$, which is of importance with regard to electronic transport. Analogously, the specific area of the interface between active material and the pore space, denoted by $S^{\mathsf{AM}\cap\mathsf{P}}$, is considered since a sufficiently large interface is required to ensure an ionic flux into the active material.

Mean chord length. A further geometrical descriptor is the chord length distribution [47, 48], where a chord is a line segment that is completely contained in a predefined phase and can not be extended further without intersecting the complementary phase. In general, the probability distribution of chord lengths depends on the orientation of the line segments. We compute the chord length distribution for the three Cartesian axes directions. In particular, for each of these three directions, we compute the mean value of the corresponding chord length distribution. In the following, the average of these three mean values, denoted by $\mu(C)$, is used.

Constrictivity. In order to explain the notion of constrictivity, we first recall the concepts of the continuous phase size distribution (CPSD) and simulated mercury intrusion porosimetry (SMIP). Namely, $\mathsf{CPSD} : [0,\infty) \to [0,1]$ is a function, where the value $\mathsf{CPSD}(r)$ is given by the volume fraction of the phase under consideration, which can be covered by (possibly overlapping) spheres with radius $r \geq 0$ such that the spheres are completely contained in the considered phase [48, 49]. Furthermore, by r_{max} the maximum radius $r > 0$ is denoted such that $\mathsf{CPSD}(r) \geq \varepsilon/2$ where ε is the volume fraction of the considered phase. The concept of SMIP is similar to that of CPSD, with the only difference that the value $\mathsf{SMIP}(r)$ of $\mathsf{SMIP} : [0,\infty) \to [0,1]$ is given by the volume fraction of the phase under consideration, which can be covered by (potentially overlapping) spheres with radius r forming an intrusion from a predefined direction. Analogously to r_{max}, by r_{min} the maximum radius $r > 0$ is denoted such that $\mathsf{SMIP}(r) \geq \varepsilon/2$. In general, r_{min} depends on the direction of the intrusion. Thus, r_{min} is computed for each of the three axes directions separately and, subsequently, the average of the three obtained values is used. The constrictivity β of the phase under consideration is then defined as $\beta = (r_{\mathsf{min}}/r_{\mathsf{max}})^2$. It is a measure for the strength of bottleneck effects and has been originally

introduced in [50]. Since $r_{\mathsf{min}} \leq r_{\mathsf{max}}$ by definition, it holds that $\beta \in [0,1]$, where $\beta = 1$ corresponds to the situation that there are no constrictions within the considered phase. In [51–53], it has been shown that the constrictivity β of the pore space has a significant impact on effective macroscopic properties of porous media such as effective diffusivity or permeability.

Mean value and standard deviation of geodesic tortuosity. A further transport-relevant geometrical descriptor is the so-called geodesic tortuosity. Besides geodesic tortuosity, there exist several other concepts of tortuosity in the literature, see e.g., [24, 54] for a comprehensive overview. According to the nomenclature proposed in [24], the geodesic tortuosity considered in the present paper corresponds to $\tau_{\mathsf{dir\_geodesic}}$. It will be denoted by τ_{g} in the following. This purely geometrical descriptor captures the windedness of transport paths, which are completely contained in a predefined phase. From 3D image data, the distribution of τ_{g} is determined by computing the lengths of shortest paths from randomly selected voxels within the considered phase, which belong to a predefined starting plane, to a parallel target plane, divided by the distance between those two planes, where shortest paths are computed using Dijkstra's algorithm [55]. Usually, the starting and target planes are chosen orthogonal to the relevant transport direction. For the image data considered in the present paper, we compute the distribution of τ_{g} with respect to each of the three Cartesian axes directions. The mean value $\mu(\tau_{\mathsf{g}})$ of τ_{g} is then determined by averaging over all shortest path lengths divided by the distance between the starting and target planes. Furthermore, the empirical standard deviation $\sigma(\tau_{\mathsf{g}})$ of these normalized path lengths is considered.

Local variants of geometrical descriptors. The computation of the geometrical descriptors stated above allows us to capture "global" morphological features of the electrodes. However, in case of lithium-ion batteries, it is well known that local heterogeneity of electrodes has a strong influence on the resulting electrochemical performance [56–59]. This is also expected to hold for polymer-based batteries, which motivates the computation of local variants of geometrical descriptors. For this purpose, the sampling window of each of the three material samples SP30, SP45 and SP60 is partitioned into non-overlapping cutouts of size $1\,\mu\mathrm{m} \times 1\,\mu\mathrm{m} \times 1\,\mu\mathrm{m}$. Next, the geometrical descriptors considered in the present paper are computed separately on each of these cutouts, which results in probability distributions of these local descriptors. In particular, Section 3.1 contains results regarding the distribution of local volume fraction as well as of the local specific surface area of interfaces.

2.5 Numerical simulation of effective transport properties

In this paper, we consider the transport of ions within the pore space and of electrons within the SuperP phase. For this purpose, we use the notion of effective tortuosity as defined in [24]. In particular, we compute the effective tortuosity as proposed in [22], which will be denoted in the following by $\tau_{\mathsf{eff}}^{\mathsf{SP}}$ for the SuperP phase, and by $\tau_{\mathsf{eff}}^{\mathsf{P}}$ for the pore space. To compute the effective tortuosities $\tau_{\mathsf{eff}}^{\mathsf{SP}}$ and $\tau_{\mathsf{eff}}^{\mathsf{P}}$ we use the segmented image data described in Section 2.3, solving the Laplace equation on either the SuperP phase or the pore space. More precisely, the Laplace problem is solved with Dirichlet boundary conditions on the top and bottom surfaces and zero flux on the side surfaces, which is a well-known computational procedure, see [60] for further details. The imposed boundary conditions determine a gradient of the solution in the main direction of electronic and ionic transport that is visualized in Figure 3.

Given the total dimensions of the samples SP30, SP45 and SP60 , see Table 2, subsamples have been considered of size not larger than $1024 \times 1024 \times 1024$ voxels, i.e., a box with a maximum length of 1024 along each axis. A list of all subsamples is given in Table 3. The FEM simulations have been performed on each of these subsamples only for the main transport direction along the y-axis (from

the current collector to the separator). These computations have been performed on the HPC-cluster HSUper (see Acknowledgments) by a finite element code based on the deal.II library [61].

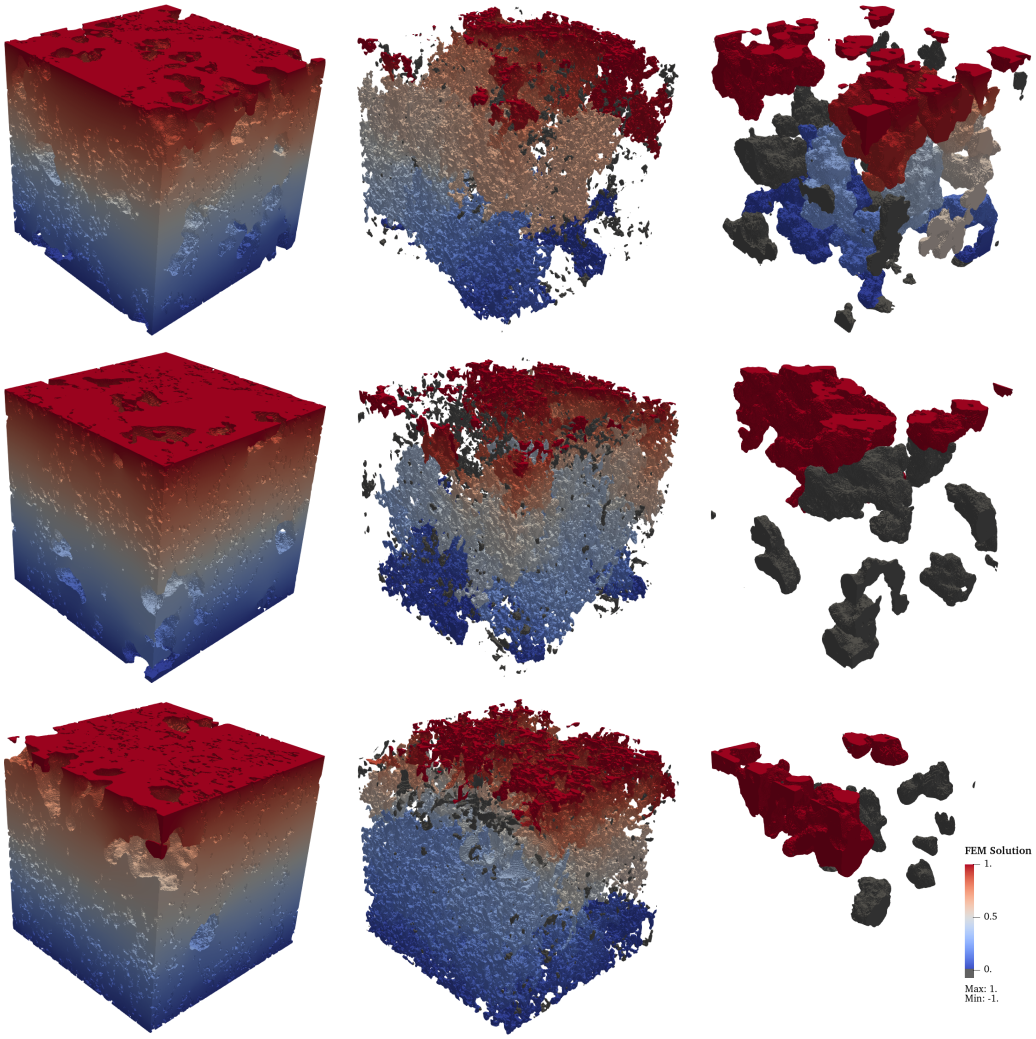

Figure 3: Visualization of the finite element solution of the transport problem to compute the effective transport coefficients in the three phases (PTMA, SuperP, pores), where the transport direction is from top to bottom, i.e. in the main direction of transport. The common color scale is shown at the right-hand side of the third row of images, where the red color corresponds to the value 1, and the blue color to 0. The gray color is used to indicate all parts that are neither connected to the top nor to the bottom surface and, therefore, do not contribute to the transport process. The electrolyte concentration in the pore space is shown in the left column, the electric potential distribution within the SuperP phase in the middle column, and the ionic concentration within PTMA in the right column. Note that the different rows correspond to the subsamples SP30.1, SP45.2 and SP60.2 (from top to bottom). In particular, the PTMA phase is not connected from top to bottom, i.e. is not percolating, in case ofsubsamples SP45.2 and SP60.2.

Homogenization of porous media uses the effective tortuosity in homogenized models to simulate the complicated transport mechanisms in these media. The broader concept of homogenization involves the transfer of microscopic processes into a macroscopic framework. In order to characterize transport phenomena in porous media using a uniform medium, adjustments to the intrinsic transport coefficients

are required. Within the context of the present paper, this adjustment is essential to account for the presence of the nano-porous structure and to ensure a more accurate representation of the transport process. In particular, effective transport coefficients D_{eff} and σ_{eff} of pore space and SuperP phase, respectively, are computed from the corresponding intrinsic coefficients as follows:

$$D_{\mathsf{eff}} = \frac{\varepsilon^{\mathsf{P}}}{\tau^{\mathsf{P}}_{\mathsf{eff}}} D, \tag{1}$$

and

$$\sigma_{\mathsf{eff}} = \frac{\varepsilon^{\mathsf{SP}}}{\tau^{\mathsf{SP}}_{\mathsf{eff}}} \sigma, \tag{2}$$

where ε is the volume fraction of the phase, on which the transport is considered. Moreover, the intrinsic diffusion coefficient and intrinsic electrical conductivity are denoted by D and σ, respectively. Note that the effective tortuosities $\tau_{\mathsf{eff}^{\mathsf{P}}}$ and $\tau_{\mathsf{eff}^{\mathsf{SP}}}$ are bounded from below by 1. Furthermore, a larger value of effective tortuosity corresponds to a more pronounced the hindering effect of the structure on the transport process. We also remark that the effective transport coefficients D_{eff} and σ_{eff} considered in Equations (1) and (2) are called M-factor in the literature [24, 51, 60]. Therefore, in the following, we will use the notations $M^{\mathsf{P}}_{\mathsf{sim}}$ and $M^{\mathsf{SP}}_{\mathsf{sim}}$ instead of D_{eff} and σ_{eff}.

Subsample	Size in x-direction	Size in y-direction	Size in z-direction	Position	Symbol
SP30.1	1024	700	1024	106,1,1	×
SP30.2	1024	700	1024	106,1,868	×
SP45.1	1024	700	880	1,1,1	●
SP45.2	1024	700	880	773,1,1	●
SP60.1	1024	1024	1024	1,1,186	■
SP60.2	1024	1024	1024	950,1,186	■
SP60.3	1024	1024	1024	1901,1,186	■
SP60.4	1024	1024	1024	1,1099,186	■
SP60.5	1024	1024	1024	950,1099,186	■
SP60.6	1024	1024	1024	1901,1099,186	■

Table 3: Information regarding the subsamples containing (from left to right): Name of the subsample, size of the subsample in x-, y- and z-direction (in number of voxels), the position of the lower left voxel of the subsample with respect to the corresponding sample, and a unique symbol as visual identifier.

3 Results and discussion

This section covers the quantitative comparison of the three polymer-based electrode samples SP30, SP45 and SP60 with regard to their 3D morphology in Section 3.1, with special emphasis on the anaslysis of local heterogeneity in Section 3.2, as well as the investigation of microstructure-property relationships in Section 3.3, where geometrical descriptors are used to predict effective transport properties by means of analytical regression formulas.

3.1 Statistical analysis of nanostructure via subsamples

To quantitatively compare the electrode samples SP30, SP45 and SP60, the geometrical descriptors stated in Section 2.4 are computed for all subsamples (see Table 3 for further information regarding

the subsamples). The obtained results are shown in Figure 4. In particular, it turned out that the volume fractions ε^{P} and $\varepsilon^{\mathsf{SP}}$ of pore space and SuperP phase are in the ranges of $[0.70, 0.81]$ and $[0.10, 0.23]$, respectively. Notably, the analyzed subsamples extracted from the three FIB-SEM images exhibit a large variability with regard to the porosity, even within the subsamples corresponding to a given sample. This effect is even more pronounced with respect to the volume fraction of the SuperP phase. In general, this kind of behavior is also observed with regard to other geometrical descriptors and the M-factor as well, which indicates a pronounced heterogeneity of the nanostructure of the electrode samples SP30, SP45 and SP60.

Furthermore, the specific surface area of the pore space (S_{P}) as well as the SuperP phase (S_{SP}) is significantly higher for the sample SP60 compared to the other two samples as shown in the second column of Figure 4. This is surprising, since there is no significant difference in specific surface area when comparing SP30 and SP45 despite these two samples differ with regard to their weight percentage of SuperP just as much as the samples SP45 and SP60.

The mean chord length ($\mu(C)$), as depicted in the third column of Figure 4, exhibits a strong correlation with the volume fraction of the respective phase, indicated by correlation coefficients of 0.77 (pore space) and 0.96 (SuperP phase), respectively. Moreover, this characteristic also - similar to the specific surface area - indicates a finer structure of the pore space as well as the SuperP phase in case of SP60 compared to SP30 and SP45.

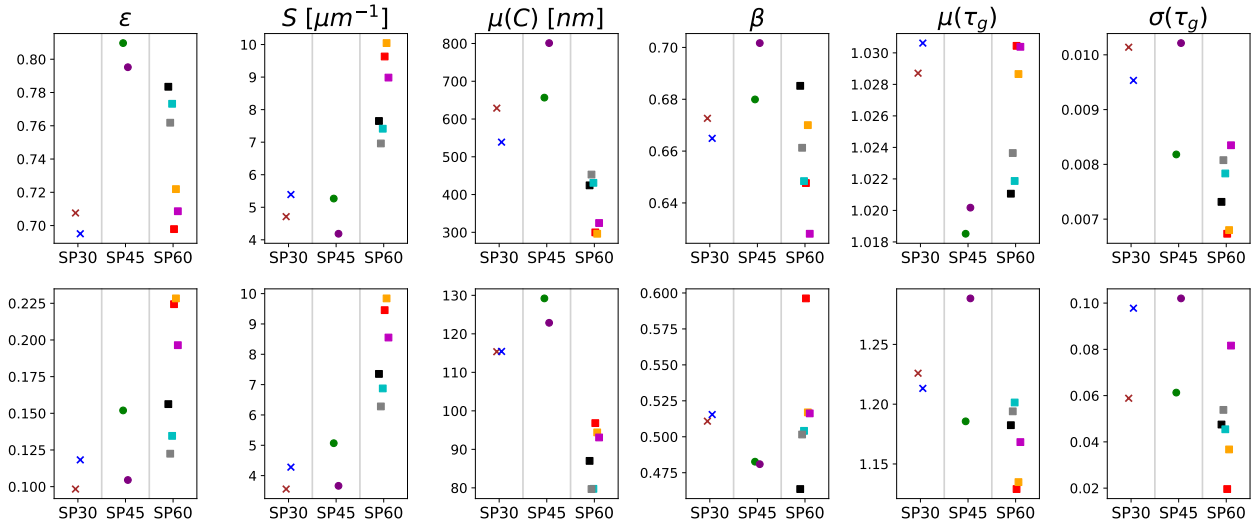

Figure 4: Morphological characterization of subsamples of the polymer-based electrodes SP30, SP45 and SP60. The columns correspond to the geometrical descriptors stated in Section 2.4. The results shown in the upper row concern the pore space, whereas the lower row refers to the SuperP phase. The shapes and colors relate to the sample and subsample symbols as given in Table 3, respectively.

With regard to the SuperP phase, there is a high variation of constrictivity within the considered subsamples only in case of sample SP60, see Figure 4. Compared to the mean chord length, the constrictivity of the respective phases is less correlated with the volume fraction. More precisely, the values of these two descriptors have a correlation coefficient of 0.58 for the pore phase and 0.55 in case of the SuperP phase. Therefore, a multi-parameter formula for predicting the M-factor in Section 3.3 that incorporates both ε and β is considered more promising than a formula based solely on ε.

With regard to the mean geodesic tortuosity of the pore space, there is no significant difference between the samples. In particular, note the small range of values in the corresponding plots shown in Figure 4. This is likely to be caused by the high porosity values, which typically ensure almost straight transport paths for ions. With regard to the SuperP phase, the situation is different. More precisely, due to the volume fractions of SuperP between 10% and 23%, the normalized lengths of shortest transport paths within the SuperP phase are significantly larger than one and differ both with regard to the three samples as well as between individual subsamples. The latter effect is most pronounced with regard to both subsamples of SP45. Besides mean geodesic tortuosity, the standard deviation of geodesic tortuosity is also considered as one possible descriptor that quantifies the local heterogeneity of the nanostructure. For example, the two subsamples of SP30 have a similar value of $\mu(\tau_g)$, but show a clear difference with regard to $\sigma(\tau_g)$. Moreover, the low correlation between $\sigma(\tau_g)$ and $\mu(\tau_g)$ as well as ε indicates that a combination of these three quantities is well suited for predicting the M-factor, see Equation (6) below.

3.2 Analysis of local heterogeneity

Besides the computation of geometrical descriptors on each subsample, we also consider the distribution of local volume fraction for each of the three phases (PTMA, SuperP, pores) to quantify the local heterogeneity of electrodes. For this purpose, non-overlapping cutouts with a size of $1\,\mu m \times 1\,\mu m \times 1\,\mu m$ are used as described in Section 2.4. The results obtained for the distribution of local volume fraction are shown in Figure 5. In particular, the three electrodes (SP30, SP45, SP60) exhibit clearly different distributions of local porosity with regard to the mean porosity, which is expected due to the different material compositions, as well as with regard to the shape of the distribution. For example, in case of SP30 there exists a significant amount of cutouts with a porosity between 50% and 60%, whereas SP45 consists mainly of regions with porosity values larger than 70%. The center plot of Figure 5 shows that for each of the three samples, there exists several cutouts that do not consist of SuperP at all, which is most pronounced in case of sample SP30. Furthermore, the spatial distribution of the active material is far from homogeneous, indicated by the plot on the right-hand side of Figure 5. More precisely, the vast majority of cutouts lack any active material when considering the samples SP45 and SP60, while those containing it can exhibit volume fractions up to 100%. In particular, the nanoparticles used for synthesizing the active material via emulsion polymerization agglomerate to large clusters, which correspond to local PTMA volume fractions close to 100% [35].

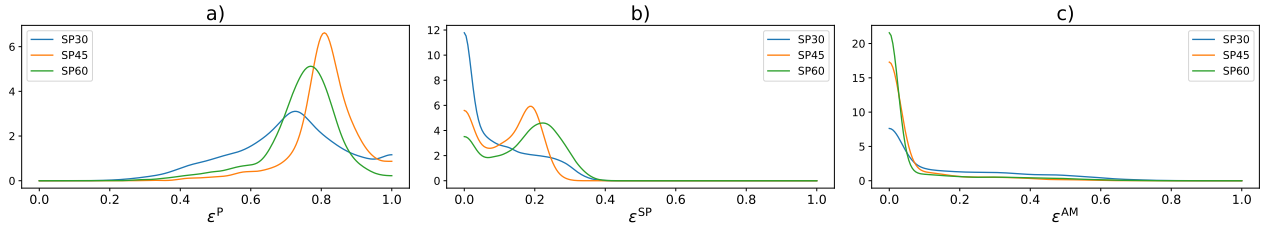

Figure 5: Distribution of local volume fraction of pore space (left), SuperP (center) and active material (right).

In case of SP30, the amount of cutouts without active material is significantly lower. More precisely, the fraction of cutouts that do not contain any active material equals 13% (SP30), 56% (SP45) and 52% (SP60), respectively.

The interface area between PTMA and the other two phases is of great importance with regard to electrochemical performance, see the plot on the left-hand side of Figure 6. Notably, a majority of the active material surface is covered by the pore space. In particular, in case of sample SP30, the interface area between active material and the SuperP phase is - in absolute numbers - the largest compared to the other two samples, even though SP30 is the sample that contains the least amount of SuperP. Moreover, the plot on the right-hand side of Figure 6 shows the distribution of the (local) ratio of the specific interface area between active material and pore space ($S^{\mathsf{AM}\cap\mathsf{P}}$) divided by the (entire) specific surface area of active material (S^{AM}). More precisely, this ratio is computed for each of the non-overlapping cutouts with a size of $1\,\mu\text{m} \times 1\,\mu\text{m} \times 1\,\mu\text{m}$ to investigate the spatial distribution of interfaces. However, there are almost no local volumes (except in the case of SP30) where there is no contact between the active material phase and the SuperP phase at all, a crucial property for a proper functioning of the electrode. Moreover, sample SP60 exhibits a non-negligible amount of regions, where the interface between pore space and active material only makes up for 40 to 70% of the (entire) specific surface area of active material, which in turn results in a comparatively large contact area between SuperP and active material.

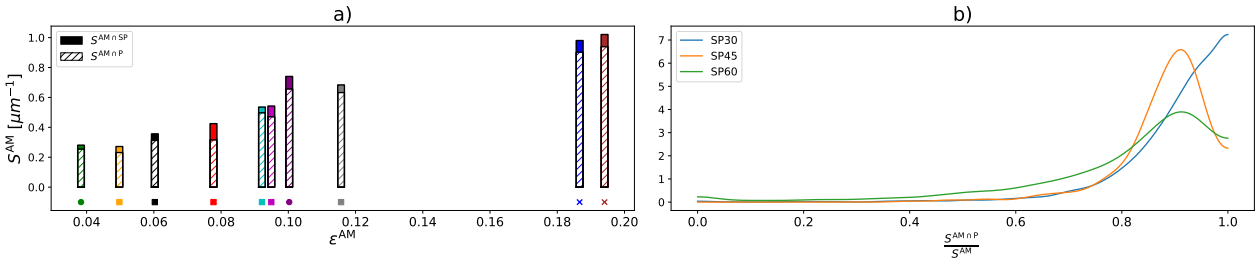

Figure 6: Left: Specific surface area of active material including the contribution of the interface between PTMA and the SuperP phase (filled part) and the interface between PTMA and the pore space (shaded part). Right: Distribution of the local ratio of the specific interface area between active material and pore space divided by the (entire) specific surface area of active material.

Finally, we consider the geodesic tortuosity of the three electrode phases in more detail, see Figure 7 which depicts the distribution of local geodesic tortuosity of the different phases and samples. In particular, it can be observed that there is no path within the active material phase between the two opposing planes in case of samples SP45 and SP60, which is not necessarily required for a proper functioning of the electrode. Furthermore, in terms of pore space and SuperP phase, SP30 and SP60 exhibit a high degree of similarity. However, with regard to SP45, the shortest paths in the pore space tend to be slightly shorter, while in the SuperP phase, they tend to be slightly longer compared to the other samples.

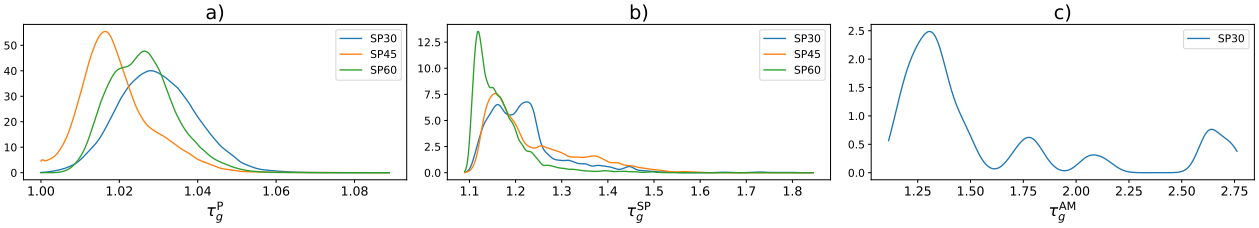

Figure 7: Distribution of local geodesic tortuosity of pore space (left), SuperP (center) and active material (right). Note that in case of the active material phase, there are no shortest paths from the starting plane to the opposite plane in case of SP45 and SP60.

3.3 Microstructure-property relationships

In addition to the computation of geometrical descriptors, FEM simulations have been performed, as stated in Section 2.5, in order to determine the effective tortuosity and the M-factor of SuperP phase and pore space for all subsamples considered in the present paper, see Table 4.

Subsample	ε^{P}	$\tau_{\mathsf{eff}}^{\mathsf{P}}$	$M_{\mathsf{sim}}^{\mathsf{P}}$	$\varepsilon^{\mathsf{SP}}$	$\tau_{\mathsf{eff}}^{\mathsf{SP}}$	$M_{\mathsf{sim}}^{\mathsf{SP}}$	Symbol
SP30.1	0.71	1.19	0.60	0.10	6.14	0.02	×
SP30.2	0.70	1.21	0.58	0.12	5.38	0.02	×
SP45.1	0.81	1.12	0.72	0.15	3.75	0.04	●
SP45.2	0.80	1.13	0.70	0.10	7.03	0.01	●
SP60.1	0.78	1.21	0.65	0.16	6.06	0.03	■
SP60.2	0.76	1.23	0.62	0.12	6.02	0.02	■
SP60.3	0.77	1.22	0.63	0.13	6.09	0.02	■
SP60.4	0.70	1.36	0.51	0.22	3.64	0.06	■
SP60.5	0.72	1.33	0.54	0.23	3.40	0.07	■
SP60.6	0.71	1.34	0.20	0.20	4.03	0.05	■

Table 4: Effective tortuosity and M-factor of pore space and SuperP phase obtained by FEM simulations, together with the volume fraction of the corresponding phase.

We now investigate the relationship between various geometrical descriptors and the M-factor of the SuperP phase and the pore space, respectively. Note that in the literature, many formulas have been considered for predicting the M-factor of various materials and different modes of transport from geometrical descriptors [53, 62, 63]. In the present paper, we discuss four of these formulas, which have demonstrated significant predictive power for both the pore space and SuperP phase with respect to the deviation measures MAPE and R^2. Recall that the mean absolute percentage error (MAPE) is given by

$$\mathsf{MAPE}(y, \widehat{y}) = \frac{1}{n} \sum_{i=1}^{n} \frac{|y_i - \widehat{y}_i|}{|y_i|}$$

where $\widehat{y} = (\widehat{y}_1, \ldots, \widehat{y}_n)$ is an n-dimensional vector of predictions of some "ground truth" data $y = (y_1, \ldots, y_n)$. A further deviation measure is the coefficient of determination (R^2) which is defined as

$$\mathsf{R}^2(y, \widehat{y}) = 1 - \frac{\frac{1}{n}\sum_{i=1}^{n}(y_i - \widehat{y}_i)^2}{\frac{1}{n}\sum_{i=1}^{n}(y_i - \overline{y})^2}, \qquad \text{where } \overline{y} = \tfrac{1}{n}\textstyle\sum_{i=1}^{n} y_i.$$

The first formula for predicting the M-factor relies solely on the volume fraction ε of the respective phase, i.e., we consider the predictor $\widehat{M}_1$ given by

$$\widehat{M}_1 = \varepsilon^{c_1}, \tag{3}$$

where $c_1 > 1$ is some constant. In the literature, various numerical values have been proposed for c_1, ranging from 1.5 (Marshall formula) to 2 (Buckingham formula) [64–66]. The value of $c_1 = 1.71$ proposed in [62] achieved the best results for the data considered in the present paper, in terms of both MAPE and R^2, and will therefore be used in the following.

The second formula provides the predictor $\widehat{M}_2$ which depends not only on the volume fraction ε of the respective phase, but also takes into account its mean geodesic tortuosity $\mu(\tau_g)$ and constrictivity β, in order to capture geometric bottleneck effects and relative path lengths. It is is given by

$$\widehat{M}_2 = \varepsilon^{c_1} \beta^{c_2} \mu(\tau_g)^{c_3}, \tag{4}$$

where $c_1 > 0, c_2, c_3 \geq 0$ are some constants. The formula given in Equation (4) was originally proposed in [63] with $(c_1, c_2, c_3) = (1.15, 0.37, -4.39)$. However, the vector of constants $(c_1, c_2, c_3) = (1, 0, -8.45)$, which was later proposed in [51], turned out to be a better choice for predicting the M-factor of the data considered in the present paper and will therefore be used later on.

A modified version of the formula given in Equation (4) can be found in [53]. It provides the predictor $\widehat{M}_3$ of the M-factor, where the constrictivity β appears in the exponent of the volume fraction ε as follows:

$$\widehat{M}_3 = \varepsilon^{c_1 + c_2 \beta} \mu(\tau_g)^{c_3}, \tag{5}$$

with some constants c_1, c_2, c_3 such that $c_1 + c_2 \geq 0, c_3 \leq 0$. In the following we consider the numerical values $(c_1, c_2, c_3) = (1.25, -1.25, -7.82)$ which have been proposed in [51].

Finally, a formula is considered which has been introduced in [67] and provides a further predictor (denoted by $\widehat{M}_4$) for the M-factor. It assesses the impact of the pore structure on the M-factor by considering the standard deviation of the geodesic tortuosity $\sigma(\tau_g)$ instead of the constrictivity β. More precisely, the predictor $\widehat{M}_4$ is given by

$$\widehat{M}_4 = c_1 \mu(\tau_g)^{c_2} \sigma(\tau_g)^{c_3} \varepsilon^{c_4}, \tag{6}$$

where the choice $(c_1, c_2, c_3, c_4) = (1.18, -9.17, 0.03, 1.02)$ of the constants c_1, c_2, c_3, c_4 proposed in [51] yields an improved fit of the M-factor for the data considered in the present paper, compared to the numerical values of c_1, c_2, c_3, c_4 derived in [67].

3.4 Evaluation of prediction power

Using the formulas given in Equations (3) to (6) for predicting the M-factor, with values for the constants c_1, c_2, c_3, c_4 taken from literature as stated above, leads to the results shown in Figure 8.

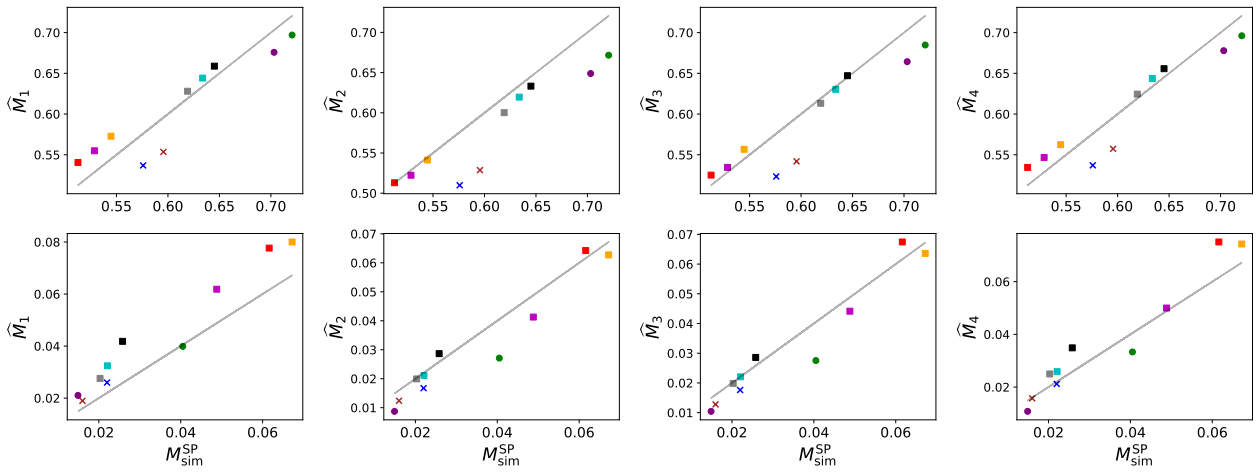

Figure 8: Prediction of M-factor via analytical regression formulas. The upper row contains the results which have been obtained for the pore space, the lower one those for the SuperP phase. The shape and color codings refer to the individual subsamples as stated in Table 3.

A quantitative evaluation of the results shown in Figure 8 in terms of MAPE and R^2 is given in Table 5. In general, one can observe an improved accuracy of the predictors of the M-factor as the number of geometrical descriptors considered in Equations (3) to (6) increases, despite the constants c_1, c_2, c_3, c_4 in these formulas being fitted in the literature to different materials and length scales. The predictors which yield the highest prediction accuracy for the data considered in the present paper, as measured by MAPE and R^2, are $\widehat{M_3}$ in case of the SuperP phase, and $\widehat{M_4}$ in case of the pore space, see Table 5. In particular with regard to the SuperP phase, $\widehat{M_3}$ clearly outperforms one of the most widely used types of predictors [51, 62, 64–66], namely $\widehat{M_1}$, which relies solely on ε. This can be explained by the fact that two material phases with a similar volume fraction can still differ significantly with regard to further (more sophisticated) geometrical descriptors as shown in Section 3.1.

Deviation measure	Phase	$\widehat{M_1}$	$\widehat{M_2}$	$\widehat{M_3}$	$\widehat{M_4}$
MAPE	pore space	0.04181	0.04622	0.03616	0.03518
R^2	pore space	0.83729	0.66458	0.80182	0.87475
MAPE	SuperP phase	0.29574	0.16464	0.13955	0.16089
R^2	SuperP phase	0.68055	0.89553	0.91235	0.87457
Involved geometr. descriptors		ε	$\varepsilon, \beta, \mu(\tau_\mathsf{g})$	$\varepsilon, \beta, \mu(\tau_\mathsf{g})$	$\varepsilon, \mu(\tau_\mathsf{g}), \sigma(\tau_\mathsf{g})$

Table 5: Quantitative comparison of prediction power of $\widehat{M_1}, \widehat{M_2}, \widehat{M_3}, \widehat{M_4}$. In each row, the highest accuracy is highlighted.

Moreover, due to the high porosity of samples SP30, SP45 and SP60, the prediction of the M-factor via $\widehat{M_2}$ and $\widehat{M_3}$, which both contain the constrictivity β, performs worse compared to $\widehat{M_4}$ since bottleneck effects within the pore space seem to be not a limiting factor. With regard to the SuperP phase, using the standard deviation of geodesic tortuosity $\sigma(\tau_\mathsf{g})$ instead of the constrictivity β leads to a significant improvement of the prediction accuracy. In particular, the predictor $\widehat{M_4}$ given by the analytical regression formula in Equation (6) is also the best performing predictor in [62], even though diffusion in loam and sand is considered in [62] at a much larger scale. This indicates that not only the mean length of shortest transport paths, but also the variability of these lengths is a well-suited geometrical descriptor for predicting diffusive properties of multi-phase materials, where the volume fraction of the transport phase is between 10 and 40%.

Furthermore, the benefit of including the standard deviation of geodesic tortuosity $\sigma(\tau_\mathsf{g})$ motivates the following consideration. A strong negative correlation between the error of the analytical regression formulas for predicting the M-factor and $\sigma(\tau_\mathsf{g})$ can be observed, i.e., we obtain a value of < -0.85 for the pore space and < -0.55 for the SuperP phase. This indicates that using this geometrical descriptor in a different manner for predicting the M-factor has the potential to further improve the prediction accuracy, which might be an interesting subject of future research.

4 Conclusions and outlook

In the present paper, three polymer-based battery electrodes (using PTMA as active material, SuperP as conductive additive and CMC as binder) are investigated by means of 3D FIB-SEM tomography, where the samples differ with regard to their material composition. To the best of our knowledge, this is the first time that the three-dimensional morphology of polymer-based batteries is quantitatively investigated in such high-resolution.

The resulting 3D image data has been segmented into active material, the union of SuperP and CMC, and the pore space. This phase-based segmentation has been then used to quantitatively

characterize the 3D morphology of the electrodes by means of geometrical descriptors. By doing so, it has been shown that there is a pronounced local heterogeneity of the electrode structure. In particular, the active material is synthesized via emulsion-polymerization resulting in nanoparticles which seem to agglomerate in the course of electrode processing from slurries. It turned out that the surface area of the active material is mostly covered by the pore space, which might result in hindered electron transport due to the comparatively low interface area between PTMA and the SuperP phase. Morevorer, the electrode sample with the highest amount of SuperP has the finest structure among the three electrodes as indicated by large surface areas and low mean chord lengths of the pore space as well as the SuperP phase.

Besides the morphological characterization of the polymer-based electrodes, effective transport properties for the ionic transport in the pore space and electronic transport in the SuperP phase have been investigated. Namely, the effective tortuosity and the effective transport coefficient, also called M-factor in the literature, have been computed for both phases and for several reference volumes. Like in the case of geometrical descriptors, a strong local variation within the electrode is observed with regard to descriptors of effective transport properties. Moreover, quantitative microstructure-property relationships are investigated to link t 3D morphology and resulting effective properties. In case of the SuperP phase, an analytical regression formula that includes the volume fraction, mean length of shortest transport paths and a bottleneck factor allows for accurate predictions of the M-factor. When considering ionic transport within the pore space instead, the porosity, the mean length of shortest transport paths and the standard deviation of geodesic tortuosity, which quantifies the local variability of the electrode structure, is able to reliably predict the M-factor. Regarding the prediction of effective electronic tortuosity of the SuperP phase, the mean absolute percentage error can more than halved by considering these more sophisticated geometrical descriptors instead of using the most widely used prediction formula that is solely based on the volume fraction.

In a forthcoming research paper, data-driven stochastic 3D microstructure modeling will be used to generate a large number of virtual, but realistic electrode structures to perform virtual materials testing for polymer-based battery electrodes. In particular, the 3D FIB-SEM data considered in the present paper allows to take the morphology of nanopores into account. Moreover, synchrotron tomography will be used to quantify spatial distribution of PTMA on a larger scale to investigate whether the regions without any active material can be considered as an outlier or are frequently occurring. The effective transport properties determined in the present paper can then be used to perform electrochemical simulations. Besides, future investigations will focus on the C-rate dependent power density, which will – similar to the energy density – be significantly affected by the electrode morphology. A further possible topic for future research is the investigation of electrodes after electrolyte filling as well as after cycling. To conclude, future research activities are required to exploit the full potential of polymer-based batteries with tailor-made microstructure as cheap, environmentally friendly energy storage technology.

Statements and declarations

Acknowledgments

The authors of the present paper are grateful to the German Research Foundation (DFG) for funding their research projects within the framework of SPP 2248 “Polymer-based batteries” (CA 633/4-1, MA 5039/7-1, SCHM 997/39-1, SCHU 1229/54-1). Computational resources (HPC-cluster HSUper) have been provided by the project hpc.bw of the Digitalization and Technology Research Center of Bundeswehr (dtec.bw), which is funded by the European Union as part of NextGenerationEU.

Competing interests

The authors have no relevant financial or non-financial interests to disclose.

Author contributions

Benedikt Prifling: Formal analysis, Writing - Original Draft, Writing - Review & Editing. Lukas Fuchs: Software, Visualization, Writing - Review & Editing. Aigerim Yessim: Software, Visualization, Writing - Review & Editing. Markus Osenberg: Visualization, Writing - Original Draft, Writing - Review & Editing, Data curation. Melanie Paulisch-Rinke: Writing - Review & Editing, Data curation. Philip Zimmer: Writing - Original Draft, Writing - Review & Editing, Resources. Martin Hager: Writing - Review & Editing. Ulrich S. Schubert: Supervision, Funding acquisition, Writing - Review & Editing. Ingo Manke: Supervision, Funding acquisition, Writing - Review & Editing. Thomas Carraro: Supervision, Funding acquisition, Writing - Original Draft, Writing - Review & Editing. Volker Schmidt: Supervision, Funding acquisition, Writing - Review & Editing.

Data availability

The data is available from the authors upon reasonable request.

References

[1] R. Korthauer, *Lithium-Ion Batteries: Basics and Applications*. Springer, 2018.

[2] B. Scrosati, K. M. Abraham, W. van Schalkwijk, and J. Hassoun, eds., *Lithium Batteries: Advanced Technologies and Applications*. The Electrochemical Society Series, J. Wiley & Sons, 2013.

[3] P. Poizot and F. Dolhem, "Clean energy new deal for a sustainable world: From non-CO_2 generating energy sources to greener electrochemical storage devices" *Energy & Environmental Science*, 4, 2003–2019, 2011.

[4] G. Liu, S. Xun, N. Vukmirovic, X. Song, P. Olalde-Velasco, H. Zheng, V. S. Battaglia, L. Wang, and W. Yang, "Polymers with tailored electronic structure for high capacity lithium battery electrodes" *Advanced Materials*, 23, 4679–4683, 2011.

[5] Z. Song and H. Zhou, "Towards sustainable and versatile energy storage devices: An overview of organic electrode materials" *Energy Environmental Science*, 6, 2280–2301, 2013.

[6] C. Friebe and U. S. Schubert, "High-power-density organic radical batteries" *Topics in Current Chemistry*, 375, 1–35, 2017.

[7] M. D. Hager, B. Esser, X. Feng, W. Schuhmann, P. Theato, and U. S. Schubert, "Polymer-based batteries – flexible and thin energy storage systems" *Advanced Materials*, 32, 2000587, 2020.

[8] K. Nakahara, J. Iriyama, S. Iwasa, M. Suguro, M. Satoh, and E. J. Cairns, "Al-laminated film packaged organic radical battery for high-power applications" *Journal of Power Sources*, 163, 1110–1113, 2007.

[9] K. Nakahara, K. Oyaizu, and H. Nishide, "Organic radical battery approaching practical use" *Chemistry Letters*, 40, 222–227, 2011.

[10] K. Nakahara, S. Iwasa, M. Satoh, Y. Morioka, J. Iriyama, M. Suguro, and E. Hasegawa, "Rechargeable batteries with organic radical cathodes" *Chemical Physics Letters*, 359, 351–354, 2002.

[11] H. Nishide, S. Iwasa, Y.-J. Pu, T. Suga, K. Nakahara, and M. Satoh, "Organic radical battery: Nitroxide polymers as a cathode-active material" *Electrochimica Acta*, 50, 827–831, 2004.

[12] NEC Corporation, "NEC develops ultra-thin organic radical battery compatible with IC cards" 2012. `https://www.nec.com/en/press/201203/global_20120305_04.html` [Accessed: 04.03.2024].

[13] Evonik Industries AG, "Evonik sells TAeTTOOz® materials technology to InnovationLab" 2022. `https://corporate.evonik.com/en/evonik-sells-taettooz-materials-technology-to-innovationlab-173925.html` [Accessed: 04.03.2024].

[14] H. Hamed, S. Yari, J. D'Haen, F. U. Renner, N. Reddy, A. Hardy, and M. Safari, "Demystifying charge transport limitations in the porous electrodes of lithium-ion batteries" *Advanced Energy Materials*, 10, 2002492, 2020.

[15] J. Moškon, S. Drvarič Talian, R. Dominko, and Gaberščček, "Advances in understanding Li battery mechanisms using impedance spectroscopy" *Journal of Electrochemical Science and Engineering*, 10, 79–93, 2020.

[16] S. N. Eliseeva, M. A. Kamenskii, E. G. Tolstopyatova, and V. V. Kondratiev, "Effect of combined conductive polymer binder on the electrochemical performance of electrode materials for lithium-ion batteries" *Energies*, 13, 2163, 2020.

[17] L. Kraft, J. B. Habedank, A. Frank, A. Rheinfeld, and A. Jossen, "Modeling and simulation of pore morphology modifications using laser-structured graphite anodes in lithium-ion batteries" *Journal of The Electrochemical Society*, 167, 013506, 2020.

[18] R. Gonçalves, S. Lanceros-Méndez, and C. M. Costa, "Electrode fabrication process and its influence in lithium-ion battery performance: State of the art and future trends" *Electrochemistry Communications*, 135, 107210, 2022.

[19] M. Chouchane and A. A. Franco, "Deconvoluting the impacts of the active material skeleton and the inactive phase morphology on the performance of lithium ion battery electrodes" *Energy Storage Materials*, 47, 649–655, 2022.

[20] S. Hein, T. Danner, D. Westhoff, B. Prifling, R. Scurtu, L. Kremer, A. Hoffmann, A. Hilger, M. Osenberg, I. Manke, M. Wohlfahrt-Mehrens, V. Schmidt, and A. Latz, "Influence of conductive additives and binder on the impedance of lithium-ion battery electrodes: Effect of morphology" *Journal of The Electrochemical Society*, 167, 013546, 2020.

[21] H.-H. Ryu, S.-B. Lee, C. S. Yoon, and Y. Sun, "Morphology-dependent battery performance of Ni-rich layered cathodes: Single-crystal versus refined polycrystal" *ACS Energy Letters*, 7, 3072–3079, 2022.

[22] M. Neumann, M. Ademmer, M. Osenberg, A. Hilger, F. Wilde, S. Münch, M. D. Hager, U. S. Schubert, I. Manke, and V. Schmidt, "3D microstructure characterization of polymer battery electrodes by statistical image analysis based on synchrotron X-ray tomography" *Journal of Power Sources*, 542, 231783, 2022.

[23] P. Zimmer, C. Stolze, S. Münch, W. Xiao, S. Stumpf, S. Höppener, M. D. Hager, and U. S. Schubert, "Percolation investigation of organic radical battery electrodes and its crucial impact on capacity utilization" *Chemical Engineering Journal*, 477, 146882, 2023.

[24] L. Holzer, P. Marmet, M. Fingerle, A. Wiegmann, M. Neumann, and V. Schmidt, *Tortuosity and Microstructure Effects in Porous Media: Classical Theories, Empirical Data and Modern Methods*. Springer International Publishing, 2023.

[25] B. Tjaden, D. J. Brett, and P. R. Shearing, "Tortuosity in electrochemical devices: A review of calculation approaches" *International Materials Reviews*, 63, 47–67, 2018.

[26] J. Landesfeind, M. Ebner, A. Eldiven, V. Wood, and H. A. Gasteiger, "Tortuosity of battery electrodes: Validation of impedance-derived values and critical comparison with 3D tomography" *Journal of The Electrochemical Society*, 165, A469–A476, 2018.

[27] J. Fu, H. R. Thomas, and C. Li, "Tortuosity of porous media: Image analysis and physical simulation" *Earth-Science Reviews*, 212, 103439, 2021.

[28] M. Doyle, T. F. Fuller, and J. Newman, "Modeling of galvanostatic charge and discharge of the lithium/polymer/insertion cell" *Journal of The Electrochemical Society*, 140, 1526–1533, 1993.

[29] M. Doyle, T. F. Fuller, and J. Newman, "Erratum: Modeling of galvanostatic charge and discharge of the lithium/polymer/insertion cell [J. Electrochem. Soc. , 140 , 1526 (1993)]" *Journal of The Electrochemical Society*, 165, X13, 2018.

[30] T. F. Fuller, M. Doyle, and J. Newman, "Simulation and optimization of the dual lithium ion insertion cell" *Journal of The Electrochemical Society*, 141, 1–9, 1994.

[31] G. W. Richardson, J. M. Foster, R. Ranom, C. P. Please, and A. M. Ramos, "Charge transport modelling of lithium-ion batteries" *European Journal of Applied Mathematics*, 33, 983–1031, 2021.

[32] F. B. Planella, W. Ai, A. M. Boyce, A. Ghosh, I. Korotkin, S. Sahu, V. Sulzer, R. Timms, T. G. Tranter, M. Zyskin, S. J. Cooper, J. S. Edge, J. M. Foster, M. Marinescu, B. Wu, and G. Richardson, "A continuum of physics-based lithium-ion battery models reviewed" *Progress in Energy*, 4, 042003, 2022.

[33] A. Innocenti, I. A. Moisés, J.-F. Gohy, and S. Passerini, "A modified Doyle-Fuller-Newman model enables the macroscale physical simulation of dual-ion batteries" *Journal of Power Sources*, 580, 233429, 2023.

[34] A. Innocenti, I. A. Moisés, O. Lužanin, J. Bitenc, J.-F. Gohy, and S. Passerini, "Practical cell design for PTMA-based organic batteries: An experimental and modeling study" *ACS Applied Materials & Interfaces*. Published online: https://doi.org/10.1021/acsami.3c1183.

[35] S. Münch, P. Gerlach, R. Burges, M. Strumpf, S. Höppener, A. Wild, A. Lex-Balducci, A. Balducci, J. C. Brendel, and U. S. Schubert, "Emulsion polymerizations for a sustainable preparation of efficient TEMPO-based electrodes" *ChemSusChem*, 14, 449–455, 2021.

[36] J. Banhart, *Advanced Tomographic Methods in Materials Research and Engineering*. Oxford University Press, 2008.

[37] K. Höflich, G. Hobler, F. I. Allen, T. Wirtz, G. Rius, L. McElwee-White, A. V. Krasheninnikov, M. Schmidt, I. Utke, N. Klingner, M. Osenberg, R. Córdoba, F. Djurabekova, I. Manke, P. Moll, M. Manoccio, J. M. De Teresa, L. Bischoff, J. Michler, O. De Castro, A. Delobbe, P. Dunne,

O. V. Dobrovolskiy, N. Frese, A. Gölzhäuser, P. Mazarov, D. Koelle, W. Möller, F. Pérez-Murano, P. Philipp, F. Vollnhals, and G. Hlawacek, "Roadmap for focused ion beam technologies" *Applied Physics Reviews*, 10, 041311, 2023.

[38] J. Schindelin, I. Arganda-Carreras, E. Frise, V. Kaynig, M. Longair, T. Pietzsch, S. Preibisch, C. Rueden, S. Saalfeld, B. Schmid, J.-Y. Tinevez, D. J. White, V. Hartenstein, K. Eliceiri, P. Tomancak, and A. Cardona, "Fiji: An open-source platform for biological-image analysis" *Nature Methods*, 9, 676–682, 2012.

[39] D. G. Lowe, "Distinctive image features from scale-invariant keypoints" *International Journal of Computer Vision*, 60, 91–110, 2004.

[40] A. Buades, B. Coll, and J.-M. Morel, "A non-local algorithm for image denoising" in *Proceedings of the IEEE Computer Society Conference on Computer Vision and Pattern Recognition*, vol. 2, 60–65, IEEE Computer Society, 2005.

[41] O. Ronneberger, P. Fischer, and T. Brox, "U-Net: Convolutional networks for biomedical image segmentation" in *Medical Image Computing and Computer-Assisted Intervention – MICCAI 2015* (N. Navab, J. Hornegger, W. M. Wells, and A. F. Frangi, eds.), 234–241, Springer International Publishing, 2015.

[42] M. Osenberg, A. Hilger, M. Neumann, A. Wagner, N. Bohn, J. R. Binder, V. Schmidt, J. Banhart, and I. Manke, "Classification of FIB/SEM-tomography images for highly porous multiphase materials using random forest classifiers" *Journal of Power Sources*, 570, 233030, 2023.

[43] S. Berg, D. Kutra, T. Kröger, C. N. Strähle, B. X. Kausler, C. Haubold, M. Schiegg, J. Ales, T. Beier, M. Rudy, K. Eren, J. I. Cervantes, B. Xu, F. Beuttenmüller, A. Wolny, C. Zhang, U. Köthe, F. A. Hamprecht, and A. Kreshuk, "ilastik: Interactive machine learning for (bio)image analysis" *Nature Methods*, 16, 1226–1232, 2019.

[44] N. Otsu, "A threshold selection method from gray-level histograms" *IEEE Transactions on Systems, Man, and Cybernetics*, 9, 62–66, 1979.

[45] S. N. Chiu, D. Stoyan, W. S. Kendall, and J. Mecke, *Stochastic Geometry and its Applications*. J. Wiley & Sons, 3rd ed., 2013.

[46] K. Schladitz, J. Ohser, and W. Nagel, "Measuring intrinsic volumes in digital 3D images" in *13th International Conference on Discrete Geometry for Computer Imagery* (A. Kuba, L. Nyúl, and K. Palágyi, eds.), 247–258, Springer, 2007.

[47] G. Matheron, *Random Sets and Integral Geometry*. J. Wiley & Sons, 1975.

[48] J. Serra, *Image Analysis and Mathematical Morphology*. Academic Press, 1982.

[49] P. Soille, *Morphological Image Analysis: Principles and Applications*. Springer, 2nd ed., 2013.

[50] B. Münch and L. Holzer, "Contradicting geometrical concepts in pore size analysis attained with electron microscopy and mercury intrusion" *Journal of the American Ceramic Society*, 91, 4059–4067, 2008.

[51] B. Prifling, M. Röding, P. Townsend, M. Neumann, and V. Schmidt, "Large-scale statistical learning for mass transport prediction in porous materials using 90,000 artificially generated microstructures" *Frontiers in Materials*, 8, 786502, 2021.

[52] L. Holzer, D. Wiedenmann, B. Münch, L. Keller, M. Prestat, P. Gasser, I. Robertson, and B. Grobéty, "The influence of constrictivity on the effective transport properties of porous layers in electrolysis and fuel cells" *Journal of Materials Science*, 48, 2934–2952, 2013.

[53] M. Neumann., O. Stenzel, F. Willot, L. Holzer, and V. Schmidt, "Quantifying the influence of microstructure on effective conductivity and permeability: Virtual materials testing" *International Journal of Solids and Structures*, 184, 211–220, 2020.

[54] B. Ghanbarian, A. G. Hunt, R. P. Ewing, and M. Sahimi, "Tortuosity in porous media: A critical review" *Soil Science Society of America Journal*, 77, 1461–1477, 2013.

[55] D. Jungnickel, *Graphs, Networks and Algorithms*. Springer, 3rd ed., 2008.

[56] M. M. Forouzan, B. A. Mazzeo, and D. R. Wheeler, "Modeling the effects of electrode microstructural heterogeneities on Li-ion battery performance and lifetime" *Journal of The Electrochemical Society*, 165, A2127–A2144, 2018.

[57] D. Kehrwald, P. R. Shearing, N. P. Brandon, P. K. Sinha, and S. J. Harris, "Local tortuosity inhomogeneities in a lithium battery composite electrode" *Journal of The Electrochemical Society*, 158, A1393–A1399, 2011.

[58] W. A. Paxton, Z. Zhong, and T. Tsakalakos, "Tracking inhomogeneity in high-capacity lithium iron phosphate batteries" *Journal of Power Sources*, 275, 429–434, 2015.

[59] S. J. Harris and P. Lu, "Effects of inhomogeneities - nanoscale to mesoscale - on the durability of Li-ion batteries" *The Journal of Physical Chemistry C*, 117, 6481–6492, 2013.

[60] M. Neumann, S. E. Wetterauer, M. Osenberg, A. Hilger, P. Gräfensteiner, A. Wagner, N. Bohn, J. R. Binder, I. Manke, T. Carraro, and V. Schmidt, "A data-driven modeling approach to quantify morphology effects on transport properties in nanostructured NMC particles" *International Journal of Solids and Structures*, 280, 112394, 2023.

[61] D. Arndt, W. Bangerth, M. Bergbauer, M. Feder, M. Fehling, J. Heinz, T. Heister, L. Heltai, M. Kronbichler, M. Maier, P. Munch, J.-P. Pelteret, B. Turcksin, D. Wells, and S. Zampini, "The `deal.II` library, version 9.5" *Journal of Numerical Mathematics*, 31, 231–246, 2023.

[62] B. Prifling, M. Weber, N. Ray, A. Prechtel, M. Phalempin, S. Schlüter, D. Vetterlein, and V. Schmidt, "Quantifying the impact of 3D pore space morphology on soil gas diffusion in loam and sand" *Transport in Porous Media*, 149, 501–527, 2023.

[63] O. Stenzel, O. M. Pecho, L. Holzer, M. Neumann, and V. Schmidt, "Predicting effective conductivities based on geometric microstructure characteristics" *AIChE Journal*, 62, 1834–1843, 2016.

[64] R. Millington and J. Quirk, "Permeability of porous solids" *Transactions of the Faraday Society*, 57, 1200–1207, 1961.

[65] E. Buckingham, "Contributions to our knowledge of the aeration of soils" 1904. US Department of Agriculture, Bureau of Soils.

[66] T. Marshall, "The diffusion of gases through porous media" *Journal of Soil Science*, 10, 79–82, 1959.

[67] S. Barman, H. Rootzén, and D. Bolin, "Prediction of diffusive transport through polymer films from characteristics of the pore geometry" *AIChE Journal*, 65, 446–457, 2019.